



# Comparison of 1030 nm and 257 nm wavelengths for U-Pb zircon dating by femtosecond laser ablation – Inductively coupled plasma mass spectrometry with support of 3D crater imaging

François-Xavier d'Abzac\*, Catherine Noiriel, Aurélie Marquet, Stéphanie Brichau

Geosciences Environnement Toulouse, Université Paul Sabatier – IRD – CNRS UMR5563, 14 avenue Edouard Belin, 31400 Toulouse, France

## ARTICLE INFO

### Keywords:

Femtosecond laser ablation  
Wavelength  
X-ray micro-tomography  
Geochronology  
3D imaging

## ABSTRACT

Femtosecond near-infrared (NIR, 1030 nm) and near-ultraviolet (NUV, 257 nm) laser ablation (fs-LA) were evaluated for U-Pb dating of zircons using inductively coupled plasma mass spectrometry (ICP-MS). The apparent ages are in agreement with the reference ages, within expanded combined uncertainties, at both wavelengths, but NIR fs-LA produces poorer uncertainties and a  $\approx 3.5\%$  bias on the reference age of Mudtank and Plešovice zircon. The time resolved  $^{238}\text{U}$  signal intensity rises sharply and progressively decreases in NUV, whereas patterns in NIR follow progressive increase and then decrease during ablation. Synchrotron X-ray micro-tomography (XRMT) imaging of an ablated quartz permitted to link the morphology and dimensions of fs-LA craters to the performances of fs-LA-ICP-MS analyses on zircons. Average ablation rates are similar at  $3 \text{ J}\cdot\text{cm}^{-2}$  for both wavelengths. However, the ablation rate is higher in NIR at  $7 \text{ J}\cdot\text{cm}^{-2}$  than in NUV at  $2 \text{ J}\cdot\text{cm}^{-2}$ , whereas the fs-LA-ICP-MS yield (in counts $\cdot\text{shot}^{-1}\cdot\text{ppm}^{-1}$ ) is lower in NIR at  $7 \text{ J}\cdot\text{cm}^{-2}$  than in NUV at  $2 \text{ J}\cdot\text{cm}^{-2}$ . This paradox as well as the biased or imprecise fs-LA-ICP-MS analyses are explained by nonlinear shot-to-shot ablation in NIR compared to NUV, induced by: (i) catastrophic ablation, (ii) incubation effects, and, to a minor extent (iii) preferential ionization of U relative to Pb. Consequently, NIR fs-LA is capable of producing accurate U-Pb ages thanks to the properties of femtosecond laser matter interactions, but with a higher fluence, sample consumption and poorer statistics than those obtained with NUV fs-LA.

## 1. Introduction

Laser ablation coupled to inductively coupled plasma mass spectrometry (LA-ICP-MS) has become a leading technique for multi elements and isotopes analyses within the last thirty years. With laser systems that use nanosecond long pulses, the emission wavelength ( $\lambda$ ) of the laser has been shown to directly relate to the analytical performances of the technique [1–3]. Indeed, matter removal rate, thermal diffusion and chemical fractionation [4–8] depend on the optical and heat penetration of the laser pulse [9,10] into the irradiated volume of the sample. The smaller  $\lambda$ , the higher the optical absorption from the sample [11], the more efficient the processes of atomic bonds breaking within the irradiated volume [12–14]. Then, increasing  $\lambda$  from 193 to 266 nm decreases the optical absorption and produces larger particles ( $> 1 \mu\text{m}$ ), which results in an increase of the laser induced chemical fractionation [15,16]. With the emergence of ultra-short pulses laser ablation systems, *i.e.* with a pulse width of several hundreds of femtosecond, this knowledge has been simply transposed and femtosecond

laser ablation (fs-LA-ICP-MS) [17] has been directly compared to pre-existing nanosecond laser ablation (ns-LA-ICP-MS) [13,18,19] even though the ablation mechanisms are very different than in the nanosecond regime. In theory, fast energy delivery ( $< 1 \text{ ps}$ ) saturates the superficial atomic layers of the target in a deterministic fashion [20] and induces multiphoton ionization (MPI) [21,22], followed by ablation according to mechanisms of spallation, homogeneous nucleation, vaporization or fragmentation as described by Perez et al. [17] which are shorter in time than the average thermal diffusion rate in a solid [23]. In addition, non-linear processes affect the optical properties of the target by locally changing its refractive index [9,24], and make the irradiated volume less transmissive to pulse energy. Hence, fs-LA laser-matter interactions should eliminate most of the  $\lambda$ -dependent effects inherent to ns-LA-ICP-MS, but no study has assessed that question in detail, using different wavelengths and a single laser – ICP-MS apparatus. The improved ablation efficiency, sensitivity, precision, and wide range of potential applications have led researchers to rather focus on the optimization of fs-LA-ICP-MS using its single emission wavelength

\* Corresponding author.

E-mail address: [francois-xavier.d-abzac@u-bourgogne.fr](mailto:francois-xavier.d-abzac@u-bourgogne.fr) (F.-X. d'Abzac).

in their respective laboratory conditions. Horn et al. [25] showed that Deep-UV 196 nm is optimal for Fe isotope analysis, a result confirmed for Si isotope analysis [26]. Other works [27,28] showed that 800 nm NIR provides accurate and reproducible U-Pb ratios and Fe isotopes analysis. D'Abzac et al. [29,30] showed that NUV 266 nm fs-LA particles are similar in size and morphology to those produced with NIR fs-LA [31], for conductors and semi-conductors, which may be a hint of the similarities of fs-LA mechanisms in NIR and NUV, but was not yet conducted on comparable lasers and ICP-MS apparatuses.

Besides, Uranium-lead dating (U-Pb) is among the most widespread application of LA-ICP-MS [32,33], with increasing versatility, from zircons to high common Pb loaded minerals, e.g., baddeleyite [25], monazite [34] or apatite [35]. Measurements of < 2% (2s) uncertainty on  $^{206}\text{Pb}/^{238}\text{U}$  ages on zircons [32,36] now reach a level of relative uncertainty of about 0.5% (2s) [33]. Because of the high interest in zircon dating, a wide variety of natural reference zircons of variable U-Pb concentrations and ages are available.

Non-invasive and non-destructive 3D X-ray micro-tomography (XRMT) using synchrotron source has demonstrated its usefulness to direct visualization of 3D samples with sub-micrometric resolutions, i.e. with a voxel size up to about  $50 \times 50 \times 50 \text{ nm}^3$  [37], and has the potential for 3D imaging of the morphology of ablation craters.

In this study, we compare the analytical performances of NIR 1030 nm emission wavelength of one fs-LA system with its fourth harmonic NUV 257 nm coupled to one sector field ICP-MS. For the first time, XRMT was applied to image the ablation craters made in natural quartz to define their shape, volume and exposed surface areas, thereafter to extrapolate precise ablation patterns to zircons in order to confront them to the corresponding fs-LA-ICP-MS measurements and unravel the cause of inaccuracies and uncertainties of U-Pb dating in zircons.

## 2. Material and methods

### 2.1. Samples

Four zircon reference materials were used in this study: zircon 91500 (Kuehl Lake in Lot, Ontario, Canada) [33,38], Plešovice (Southern Bohemian Massif, Czech Republic) [39], Fish Canyon Tuff (San Juan Volcanic Field, Colorado, USA) [40] and Mudtank (Strangways Metamorphic Complex, Northern Territory, Australia) [33,41]. Table 1 reports their provenance, accepted age, radiogenic lead (Pb\*) and uranium concentrations, size of the studied crystals along the c-axis and the corresponding references. Although 3D geometry of about  $60 \times 150 \mu\text{m}^2$  zircons has been recently made available using XRMT imaging [42], imaging of craters in a 1 mm large Plešovice zircon failed to provide data of sufficient high quality due to the size of the sample regarding the high X-ray absorption of the  $\text{ZrSiO}_4$  matrix. To overcome this problem, a natural pristine quartz grain from Torres del Paine [43] of  $\sim 1 \text{ mm}$  along the c-axis and  $\sim 500 \mu\text{m}$  wide was used as an analogue to study fs-LA craters. Although the  $\text{SiO}_2$  matrix has a low X-ray absorption and high contrast with air, in the femtosecond regime, ablation mechanisms are independent on the matrix [44]. Therefore, we consider that the evolution of the crater morphology made in quartz is comparable to that of craters in zircon.

**Table 1**

Characteristics of the zircon reference materials.

Sample	Location	Age (Ma)	Pb (ppm)	U (ppm)	Size (mm)	References
91500	Canada	$1063.51 \pm 0.39$	22–135	71–86	$\approx 0.5$	[16,38]
Plešovice	Czech rep.	$337.13 \pm 0.37$	21–158	465–3084	0.5–1	[39]
Fish Canyon Tuff	USA	$28.49 \pm 0.003$	1–6	200–850	$\approx 0.05\text{--}0.1$	[41]
Mudtank	Australia	$731.65 \pm 0.49$	0.73–4.39	6.1–36.5	$\approx 10$	[33,40]

Sizes are estimations along the c-axis. Ages are determined by (chemical abrasion) – Isotope dilution – Thermo ionization mass spectrometry (CA)-ID-TIMS with 2s uncertainties.

### 2.2. Femtosecond laser ablation system

The Géosciences Environnement Toulouse laboratory is equipped with an ESI “UC Femto” femtosecond laser ablation system (Portland, OR, USA). The apparatus is composed of a chirped pulse amplification system which delivers 1030 nm NIR pulses of  $\approx 280 \text{ fs}$  width with a gaussian energy distribution. The “Dual Wave” system is a mechanical switch allowing to re-direct the fundamental NIR beam towards a fourth harmonic generator in order to convert NIR into Gaussian-shape, 257 nm NUV pulses of  $\approx 280 \text{ fs}$  with a conversion yield of  $\approx 35\%$ . The repetition rate ranges from 1 to 250 Hz. The spot size on the sample is controlled from 1 to 60  $\mu\text{m}$  using a beam imaging system, i.e. the aperture at the laser output is the object side plane of an optical system which sample surface is the image side plane. One inch polished sections are placed in a two volume cell with a wash out time < 700 ms. The aerosol is carried with helium into a 2 m PTFE-coated tubing and mixed with argon using a Y-connector about 40 cm before the plasma torch.

### 2.3. U-Pb dating

Single spots of 30  $\mu\text{m}$  diameter at 4 Hz were made with a fluence of  $2 \text{ J.cm}^{-2}$  in NUV. Two fluences needed to be set in NIR for a robust comparison: one fluence-equivalent of the NUV (noted F-eq) and one signal-equivalent to the NUV (noted S-eq). However, a  $2 \text{ J.cm}^{-2}$  fluence could not be used in IR-F-eq mode because of a too low signal intensity. Instead, the minimum fluence of  $7 \text{ J.cm}^{-2}$  for signal quantification was used. The IR-S-eq mode required  $13 \text{ J.cm}^{-2}$  to reach the signal intensity obtained in NUV. Tuning was performed as usual on NIST SRM 610 certified glass standard in NUV and rastering mode, using a spot of 20  $\mu\text{m}$  in diameter, a fluence of  $2 \text{ J.cm}^{-2}$ , a 10 Hz repetition rate and raster speed of  $10 \mu\text{m.s}^{-1}$  on masses  $^{238}\text{U}$ ,  $^{206}\text{Pb}$  and by keeping the oxide level ( $^{238}\text{U}^{16}\text{O}/^{238}\text{U}$ ) below 0.5%. In these conditions, sensitivity is reproducible around  $5.10^4 \text{ cps.ppm}^{-1}$  on  $^{238}\text{U}$ . Analyses were performed on a Thermo Element XR ICP-MS. Nine masses  $^{204}(\text{Hg} + \text{Pb})$ ,  $^{206}\text{Pb}$ ,  $^{207}\text{Pb}$ ,  $^{208}\text{Pb}$ ,  $^{232}\text{Pb}$ ,  $^{235}\text{U}$  and  $^{238}\text{U}$  were acquired in E-scan mode (i.e., without magnet jump) with a 2% mass window and 200 samples per peak. Data were processed under Iolite™ using zircon 91500 as an external standard analyzed every 5 unknowns. The data processing workflow is inspired from Horstwood et al. [33] and comprises background subtraction, downhole fractionation correction, normalization to the external standard. Statistical treatment and evaluation of the age uncertainty and MSWD of concordance are computed under IsoplotR [33]. Analytical conditions are reported in Table 2.

### 2.4. Synchrotron X-ray micro-tomography

The quartz crystal was ablated in NUV and NIR with a 40  $\mu\text{m}$  spot size at 40 Hz. This higher repetition rate was chosen in order to generate the series of craters in a shorter time. Neither the mechanism of ablation nor the shape of the craters will be different from fs-LA operated at 4 Hz since, in both cases, each pulse of < 300 fs is independent in time from the previous/next one. The slightly larger spot size was chosen in order to obtain craters that would fit better the micro-tomography imaging resolution. This will not have any influence

**Table 2**  
Setup of fs-LA-ICP-MS apparatus.

Sample	Zircon single crystals		
Preparation	One inch polished sections		
Laser ablation	ESI "Femto UC"		
Mode	NUV	NIR-F-eq	NIR-Seq
Wavelength	257 nm	1030 nm	1030 nm
Fluence	2 J.cm <sup>-2</sup>	7 J.cm <sup>-2</sup>	≈ 13 J.cm <sup>-2</sup>
Repetition rate	4 Hz	4 Hz	4 Hz
Spot diameter	30 μm	30 μm	30 μm
Pulse width	280 fs	280 fs	280 fs
Ablation cell	Two volumes (ESI)		
Sampling mode	Single spot		
Carrier gas	He: 0.3–0.55 L.min <sup>-1</sup>		
Sample gas	Ar: 1 L.min <sup>-1</sup>		
Background	15 s		
Ablation duration	25 s		
Wash-out time	11 s		
ICP-MS	Thermo Fisher "Element XR", HR-ICP-MS		
Sample introduction	Dry transport via PTFE tubing		
RF power	1280 W		
Sampler cones	H type (Ni)		
Skimmer cones	X type (Ni)		
Data acquisition	Time resolved analysis		
Scanning mode	E-scan, peak hopping, one point per peak		
Detector mode	Pulse counting, dead time correction applied, analog mode when signal intensity > 10 <sup>6</sup> cps		
Masses acquired	<sup>204</sup> (Hg + Pb), <sup>206</sup> Pb, <sup>207</sup> Pb, <sup>208</sup> Pb, <sup>232</sup> Th, <sup>235</sup> U, <sup>238</sup> U		
Integration time	300 runs, 20 ms per mass, i.e. 54 s		
Sensitivity	5.10 <sup>4</sup> cps.ppm <sup>-1</sup> on <sup>238</sup> U		
Oxide production	<sup>238</sup> U <sup>16</sup> O/ <sup>238</sup> U < 0.5%		
Data processing	Iolite™, IsoplotR		

Sensitivity was calculated from tuning using raster ablation at 10 μm.s<sup>-1</sup> speed, 10 Hz repetition rate, with a 20 μm diameter spot size and 2 J.cm<sup>-2</sup> on the NIST610 certified standard. The sensitivity during U-Pb analyses must be different because of the different laser settings used (fluence, spot size, wavelength, repetition rate). Data processing included background correction, correction of systematic bias using zircon 91500, downhole fractionation correction using a smooth spline fitting function and temporal drift using a smooth spline fitting function over sequences of ≈ 1 h. See Paton et al. [45] and Horstwood et al. [33] for details.

on the comparison with U-Pb measurements on zircons since the energy density was kept similar. Indeed, three fluences were used, including the one used for U-Pb dating on zircons, to study the morphology over a large range of LA-ICP-MS conditions, i.e., 1.1, 2.1 and 3 J.cm<sup>-2</sup> in NUV and 3, 7 and 13 J.cm<sup>-2</sup> in NIR. Each time, seven craters were generated in line with a number of shots ranging from  $N = 5$  to 1500. Imaging was carried out at the TOMCAT beamline [46], Swiss Light Source (Paul Scherer Institute, Switzerland). The data were collected with a pixel size of 0.65 μm, using a 10× magnification diffraction-limited microscope optics. Each data set is composed of 1701 radiographs collected over a 180° rotation range. Each radiograph was recorded with a monochromatic and parallel beam at 20 keV and an exposure time of 200 ms. Volume reconstruction was performed from the radiographs corrected from flat field and background noise using an algorithm based on the Fourier transform method [47]. Image processing was achieved with Avizo® software. After reconstruction, two volumes of 500 × 1000 × 200 and 600 × 1100 × 200 voxels containing the NUV or NIR craters were extracted from the sample. The 3D grayscale volumes were converted to 8-bit integers, and denoised with a 3D median filter. In addition, the volumes were registered using a linear interpolation so that the flat, polished surface of the crystal that was ablated fits with the horizontal plane. Then, the images were segmented with a region growing algorithm [48] in order to separate the solid from air and the individual craters were labeled and extracted from the 3D images. A few artifacts inherent to the imaging technique, namely ring artifacts, were removed manually. The volume of each crater was calculated from the number of voxels (a voxel is 0.65 × 0.65 × 0.65 μm<sup>3</sup>) comprised between the horizontal surface plane and the surrounding

quartz matrix. The surface area of the craters was calculated from the number of air-quartz interface pixels (a pixel is 0.65 × 0.65 μm<sup>2</sup>). The depth of the craters was defined as the longest segment normal to the initial polished quartz surface. Equivalent diameters (D) of the craters were calculated from the top surfaces extracted from the horizontal surface plane (S) following eq1. The crater aspect ratio is the depth-to-equivalent diameter ratio of each crater.

$$D = 2 \sqrt{\left(\frac{S}{\pi}\right)} \quad (1)$$

### 3. Results

#### 3.1. U-Pb dating

Concordia ages are shown in Fig. 1 with the corresponding data in Table S1 (Appendix). In NIR-F-eq, the <sup>235</sup>U signal intensity was too low to calculate a <sup>207</sup>Pb/<sup>235</sup>U age so it was derived from the <sup>238</sup>U intensity based on a 1/137.88 <sup>238</sup>U/<sup>235</sup>U abundance ratio [49]. Rejected data are highlighted in Table S1 (Appendix) and are based on high degree of shifting from the Concordia curve (> 10%) or aberrant precision on <sup>207</sup>Pb/<sup>235</sup>U (generally > 0.5% (2RSD)), except for Mudtank which error ellipses are large enough so that 10% of discordance still fits the Concordia, so the threshold was set to 30%. The latter settings are usually avoided during U-Pb analyses of such low [U] and [Pb] samples but were required for the sake of comparison in this study. All uncertainties are given as 2s (95% interval). Although zircon 91500 is the external standard, Iolite™ calculates U-Pb ages from the data by bracketing each of its measurement using their two corresponding zircon 91500 closest neighbors. Zircon 91500 ages are then accurate in the three modes. Near IR-S-eq produces a poorer relative standard deviation of 0.8% (2RSD) than NUV, even poorer in NIR-F-eq with 2.6% (2RSD).

Fish Canyon Tuff and Plešovice zircons show the same increasing uncertainties when switching to NIR modes. Still, ages are accurate except for Plešovice zircon in IR-S-eq mode with 325.22 ± 2.85 Ma, which is offset by ≈ 3.5%. Mudtank zircon has much lower U and Pb concentrations and shows higher uncertainties than the other zircons, albeit comparable in the three modes, i.e. ≈ 4% (2RSD). Concordant ages of 749.50 ± 30.10 and 709.90 ± 30.30 Ma are found with NUV and NIR-S-eq, respectively, the latter being offset by ≈ 3.5%. The NIR-F-eq setting provides an age of 810.80 ± 38.5 Ma that is highly biased from the reference age (Table 1).

#### 3.2. Crater development and fs-LA-ICP-MS

Fig. 2 shows 3D images and top-surface maps of the ablated quartz. Numerical data (volumes, surface, depth and aspect ratio) are available in Table S2 (Appendix). At 3 J.cm<sup>-2</sup> in NUV, only one 5-shots crater damaged the surface enough to be visible on the images. In NIR at 13 J.cm<sup>-2</sup>, five craters were damaged (labeled "removed volume" and "n/a" in Fig. 2) by transport and because of the weakening of the crystalline structure by multiple ablations, so that no calculation was possible. The Near IR crater borders are irregular whereas the NUV craters have rounded shapes. Near UV craters, under 500 shots, display a shallower bottom in the center than on the sides. This is due to light diffraction through the diaphragm placed at the laser output, which generates a first ring of diffraction that has a higher energy density than the center part of the beam. Diffraction also occurs in NIR but it is not imprinted on the sample surface because the longer wavelength expands the diffraction rings diameter so that their energy density is lower and only the center part of the beam provides energy for ablation. Fig. 3A shows the crater volume (in μm<sup>3</sup>) as a function of the number of shots (N) in NIR and NUV at 3 J.cm<sup>-2</sup>. The evolution of the crater is comparable between the two wavelengths. At first, a logarithmic fitting function was thought to link the crater volume to N. Unfortunately the

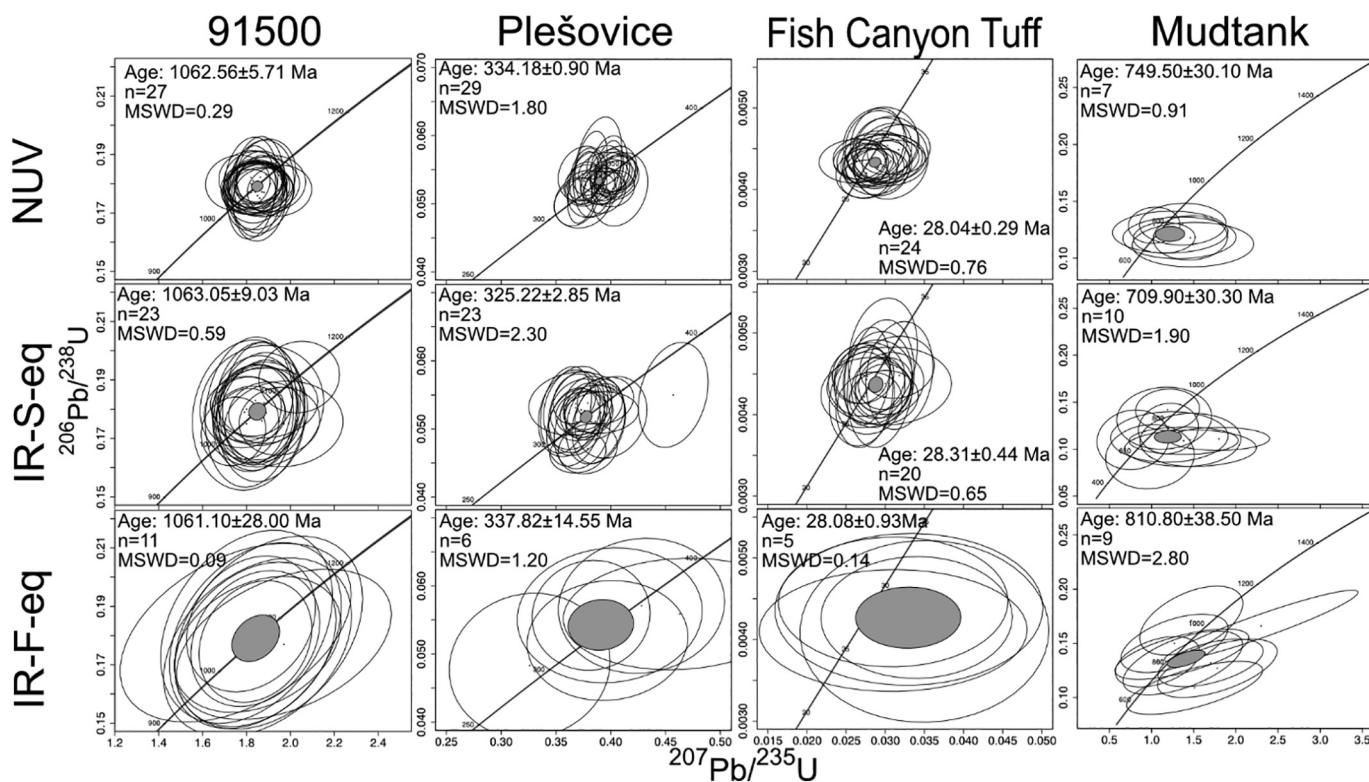


Fig. 1. Concordia diagrams of the U-Pb ages for the zircons 91500, Plešovice, Fish Canyon Tuff and Mudtank. The diagrams are presented in a double entry table with the NUV, IR-S-eq and NIR-F-eq modes. Uncertainty is 95% confidence level (2s), n is the number of data points after rejection. Data are available in Table S1.

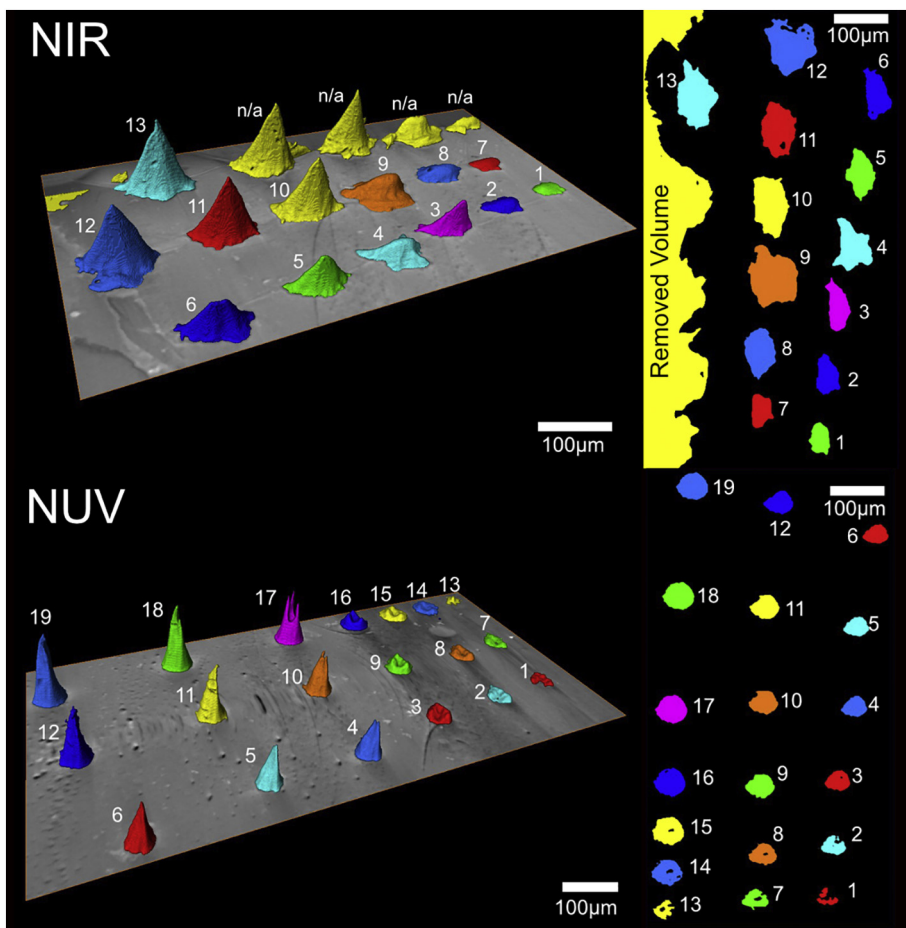


Fig. 2. 3D volume rendering of the craters (bottom-to-top) obtained from X-ray micro-tomography imaging, and 2D surface maps of the crater series made in the quartz sample in NUV (1, 2 and 3 J.cm<sup>-2</sup>) and NIR (3, 7 and 13 J.cm<sup>-2</sup>). In NUV, craters from 1 to 6, 7–12 and 14–19 result from 25, 50, 100, 500, 1000 and 1500 shots. Crater 13 is the only 5-shot ablation which resulted in a visible damage. In NIR, craters from 1 to 6 and 7–12 result from 25, 50, 100, 500, 1000 and 1500 shots. The “n/a” are associated with the “removed volume” on the 2D map and only crater 13 (1500 shots) can be characterized.

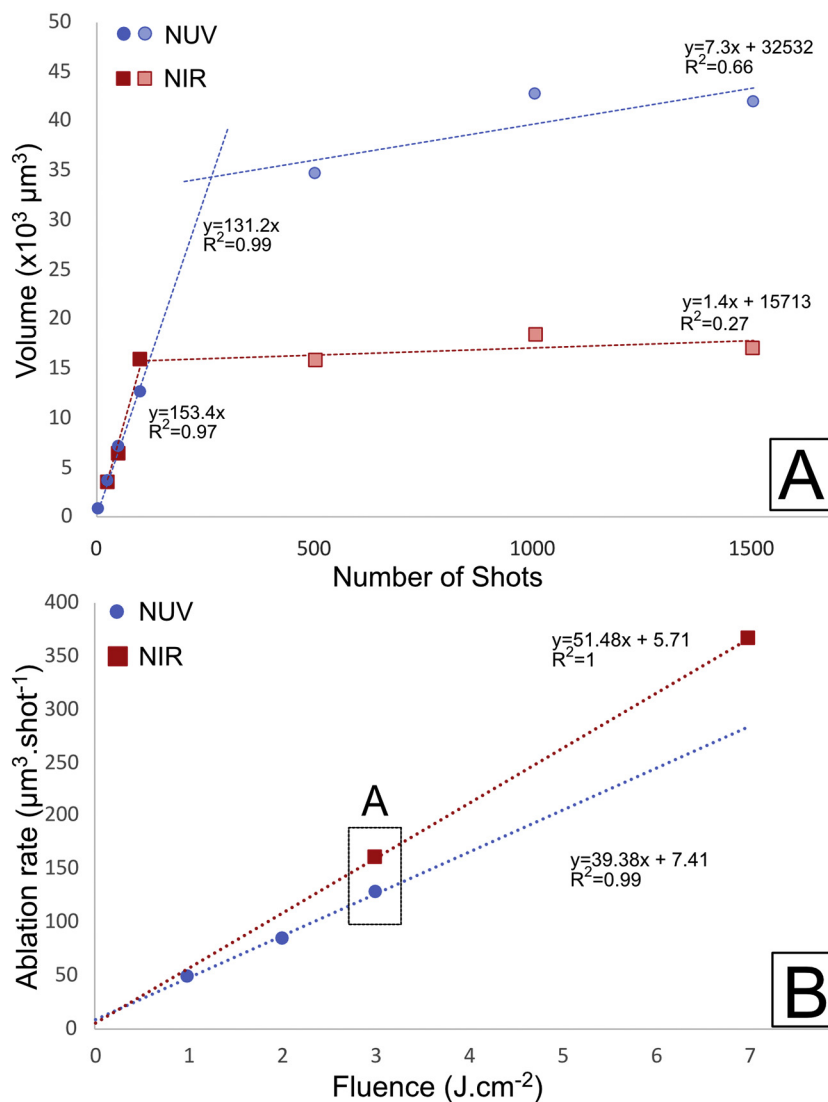
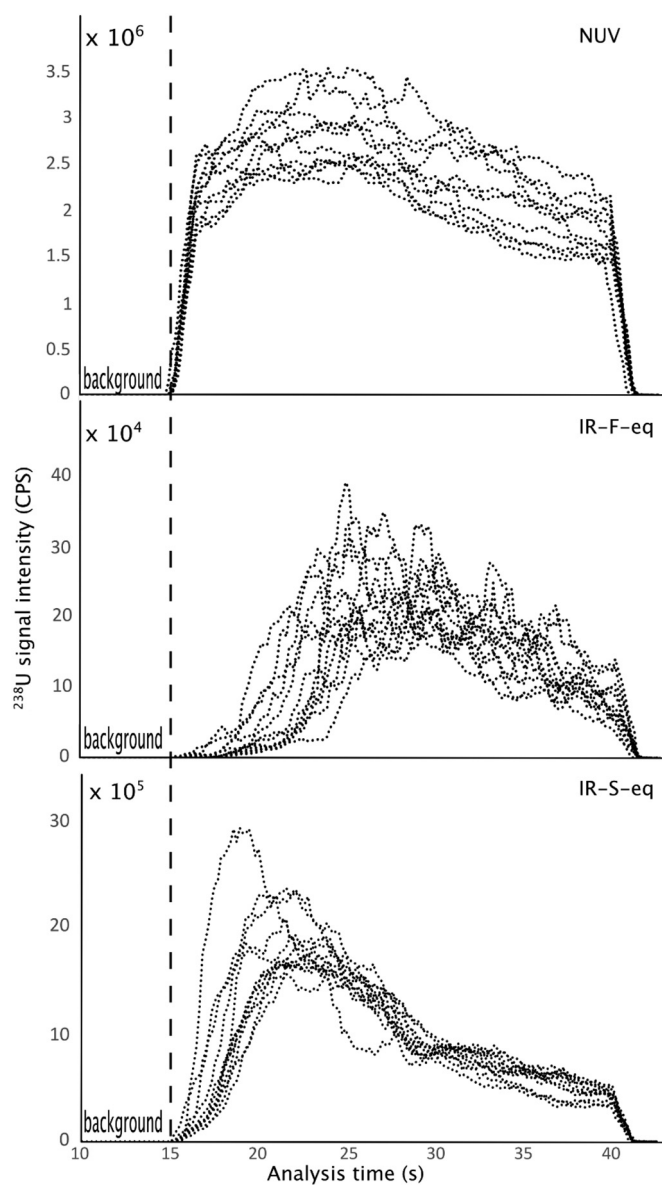


Fig. 3. A) Ablated volume (in  $\mu\text{m}^3$ ) as a function of the number of shots (N) in NUV and NIR at  $3 \text{ J} \cdot \text{cm}^{-2}$ , and the corresponding two-step linear fit, B) Evolution of the ablation rate (in  $\mu\text{m}^3 \cdot \text{shot}^{-1}$ ) as a function of fluence (in  $\text{J} \cdot \text{cm}^{-2}$ ) in NUV and NIR. The "A" area corresponds to the experimental conditions reported in A) for the first step of the fit. Volumes are calculated from 3D X-ray micro-tomography images (Table S2, Appendix).

fitting was neither satisfactory at high values of N (Fig. S1, Appendix) nor the curve did reach the origin, which is a requirement as the ablation volume should be null for zero shot. Hence a two-step fit was preferred, with the first one built over the first 100 shots and forced to the origin and the second extrapolated for higher values of N (Fig. 3A). We obtain two ablation rates from each two-step fit, expressed as the slopes of the linear extrapolations, which transition is the point at which the two linear fits are equal. During the first stage,  $< 260$  shots in NUV and  $< 103$  shots in NIR, the ablation rates are  $131.2 \mu\text{m}^3 \cdot \text{shot}^{-1}$  and  $153.4 \mu\text{m}^3 \cdot \text{shot}^{-1}$ , respectively, with linear regression coefficients  $> 0.97$ . The second stage,  $> 260$  shots in NUV and  $> 103$  shots in NIR, shows ablation rates close to near zero values, i.e.  $\approx 7 \mu\text{m}^3 \cdot \text{shot}^{-1}$  in NUV and  $\approx 1 \mu\text{m}^3 \cdot \text{shot}^{-1}$  in NIR, with poor regression coefficients. This change correlates with a loss of fluence of  $> 75\%$  to  $> 90\%$  in NUV and NIR as the irradiated area in the crater increases by factors of 10 and 4 respectively, after 500 shots (Table S2, Appendix). Fig. 3B presents the average ablation rate as a function of fluence calculated as  $V/N$  with  $N = 100$  shots. The obtained values (Table S2, Appendix) at  $3 \text{ J} \cdot \text{cm}^{-2}$  are very close to the slopes of linear extrapolations forced to the origin in Fig. 3A, which attests for the validity of the two-step fit model. The two trends show that the effect of wavelength on the ablation rate is limited below 100 shots at fluences  $< 3 \text{ J} \cdot \text{cm}^{-2}$ , since a

change of only  $\approx 33 \mu\text{m}^3/\text{shot}$  at  $3 \text{ J} \cdot \text{cm}^{-2}$  is displayed between NIR and NUV. Above, however, the rate becomes higher in NIR than in NUV.

The time-resolved evolution of the signal intensity of  $^{238}\text{U}$  throughout fs-LA-ICP-MS acquisition is represented in Fig. 4. Plešovice zircon was selected due to its higher  $^{238}\text{U}$  concentration so that the time-resolved intensity pattern is well defined and allows detailed comparisons between modes. All ablations of Plešovice of one measurement sequence in each of the three modes were superimposed and moving averages model fittings on seven data points were plotted in order to assess the signal intensity pattern of each mode. In NUV, the intensity is maximal near  $2.10^6$  cps within 5 s after ablation starts, then decreases until ablation stops. In NIR-S-eq, the intensity increases by one order of magnitude during the first 5 s of ablation and matches that of the NUV mode as set up, then decreases quickly by the same amount within the next 5 s, and finally decreases linearly until ablation stops. In NIR-F-eq, the intensity increases by one order of magnitude after 10 s of ablation, then decreases until ablation stops. The maximum intensity is 10 times lower than that obtained with the NUV mode. Finally, whereas the NUV mode exhibits sharp rises of intensity, the NIR modes have more progressive and random patterns of intensity increase, spreading between 18 s and 23 s. Fig. S2 (Appendix) complements this result with the same information for all the zircon samples in the three modes and



**Fig. 4.** Time-resolved signal intensity of  $^{238}\text{U}$  measured in Plešovice zircon in NUV, NIR-S-eq and NIR-F-eq represented as moving average model fittings of the discrete time-resolved signal intensity. All the acquisitions of a measurement run are superimposed. The ordinate scale changes between modes to emphasize the shape of the time-resolved signal. For each set up, a specific and repeatable pattern can be observed.

shows that the time-resolved signal intensity patterns are not sample-dependent. These results agree with those obtained by Borisov et al. [50] who showed time-resolved fluence-dependent patterns.

Time-resolved signals and crater geometries give access to the total fs-LA-ICP-MS yield, defined as the ICP-MS signal intensity in counts per unit of volume ( $\mu\text{m}^3$ ), normalized to the concentration of the element of interest (in ppm). We considered the comparable NUV and NIR-F-eq modes,  $^{238}\text{U}$  as the element of reference, and 4 successive fs-LA-ICP-MS measurements acquired out of a run of 60 analytes. The blank-corrected  $^{238}\text{U}$  signal intensity was integrated over 6.25 s (25 shots), 12.5 s (50 shots) and 25 s (100 shots), and plotted against the corresponding crater volumes. The slope of the linear fitting forced to origin is the raw ablation yield (in counts. $\mu\text{m}^{-3}$ ), normalized to the uranium concentration to provide the fs-LA-ICP-MS yield in counts. $\mu\text{m}^{-3}.\text{ppm}^{-1}$  U (Fig. S3). This approximation proves meaningful since all the zircons show similar values for a given mode (Table S3, Appendix). The yield of NUV

fs-LA ranges from 37.5 to 62 counts. $\mu\text{m}^{-3}.\text{ppm}^{-1}$ , which is 30 to 70 times higher for all samples than that of NIR fs-LA, for which the yield ranges from 0.5 to 1.4 counts. $\mu\text{m}^{-3}.\text{ppm}^{-1}$ . The difference is significant considering that the sensitivity (Table 2) remains constant, and the shape of the time-resolved signal is reproducible through the session (Fig. 4).

## 4. Discussion

### 4.1. Inaccurate U-Pb data

The performance differences of U-Pb dating in NIR and NUV result from differences of the crater evolution. Inaccurate ages of the Mudtank zircon in both NIR modes and Plešovice for NIR-S-eq are 25, 81 and 12 Ma off from the reference age, respectively. For Mudtank in NIR-F-eq mode, this effect could be linked to the low concentrations of  $[\text{Pb}^*]$  ( $< 0.73$  ppm) and  $[\text{U}]$  ( $< 6$  ppm), but these values are still significantly above the limit of quantification (Intensity/Background  $> 10$ ). In addition, since  $^{235}\text{U}$  is calculated from the intensity of  $^{238}\text{U}$  and apparent ages are concordant within uncertainty, inaccurate data are likely induced by a biased counting of  $^{238}\text{U}$  atoms relative to  $^{206}\text{Pb}^*$  and  $^{207}\text{Pb}^*$  atoms. On the other hand, a bias of 3.5% towards younger ages than the reference ones is observed with Mudtank and Plešovice in NIR-S-eq. This indicates that inaccurate data in NIR-S-eq are induced by fundamental ablation processes during crater development.

### 4.2. Ablation rate and wavelength

For equivalent fluences, the effect of wavelength on the ablation rate is limited. Similar rates are found at  $3 \text{ J.cm}^{-2}$  (Fig. 3A) and the crater aspect ratio remains  $< 1$  (Table S2, Appendix), which is safe for performing fs-LA without chemical fractionation due to the crater depth [50]. This shows that there is no preferential pulse energy loss through optical transmission or thermal diffusion in NIR, what Ben Yakar et al. and Le Harzic et al. [51,52] showed for semiconductors and metals. Unchanged optical transmission at all wavelengths is explained by nonlinear effects as ultra-short pulses locally modify the refraction index of the target towards less transmissive medium [53]. The effect of wavelength on the physical properties of the target appears then extremely limited against that of the ultra-short pulse width. Phenomena such as self-focusing within the solid still occur [24,54], so a small fraction of the pulse energy can be transmitted, but the data show that this effect is negligible since inaccurate data are not produced for a specific sample or wavelength. However, irregular crater shape in NIR (Fig. 2) strongly suggest that catastrophic ablation occurs as ejection of large chunks of crystal during ablation ( $> 100 \mu\text{m}$  in diameter) [55], which is not observed in NUV. Such differences should be reflected by the shape of the time resolved signal.

### 4.3. Time-resolved signal and crater development

The time-resolved signal (Fig. 4) shows more differences between the NUV and NIR modes than expected from the corresponding ablation patterns obtained with XRMT (Figs. 2 and 3). At  $7 \text{ J.cm}^{-2}$ , NIR modes are 30 to 70 times less effective than NUV at the fluence of  $2 \text{ J.cm}^{-2}$ , even though Fig. 3B predicts a higher ablation rate in NIR than in NUV at these fluences, i.e.  $400 \mu\text{m}^3.\text{shot}^{-1}$  and  $100 \mu\text{m}^3.\text{shot}^{-1}$ , respectively. This should result in a higher yield in NIR, which is not the case (Table S3, Appendix). Moreover, similar ablation rates are found over 100 shots in both NUV and NIR (Fig. 3A), whereas the corresponding time-resolved signal intensities are different (Fig. 4). The inconsistency can be explained by: i) re-deposition and losses of particles during ablation and transport, ii) incomplete ionization of particles in the ICP or iii) a nonlinear evolution of the crater during acquisition, which biases the calculated average yields. The first hypothesis requires large particles to be produced ( $> 1 \mu\text{m}$  in diameter), electrostatic deposition on the tubing walls, or particles deposition within the ablation cell [56,57].

Previous works [29,31,58] showed that the size and morphology of fs-LA particles are similar and matrix-independent in NIR and NUV, so that transport losses can be considered as equivalent for a given apparatus, which is confirmed by the correct U-Pb ages measured at both wavelengths, and the similar degree of inaccuracy between samples for a specific mode (Fig. 1). Products of catastrophic ablation in NIR can be spotted as outliers on time-resolved  $^{206}\text{Pb}/^{238}\text{U}$  signal (Fig. S3, Appendix) for random ablations of Plešovice zircon. This observation depends on the probability of large ejecta to reach the ICP, and so, is a random phenomenon, as shown by the stable  $^{206}\text{Pb}/^{238}\text{U}$  in NIR-S-eq (Fig. S4, Appendix). Hence, catastrophic ablation and transport losses cannot fully explain the systematic low yield of NIR as compared to NUV, but it certainly biases our estimation of the average ablation rate, with overestimation of the removed volume at each acquired data point. Incomplete ionization is unlikely to happen for particles as small as those produced by fs-LA [31], unless they are the result of catastrophic ablation. This hypothesis is then linked to the first one and hardly explains our results. This supports the third option of a nonlinear evolution of the crater.

The crater may evolve in a nonlinear fashion from shot to shot because of the photon energy of the laser. In fs-LA, ablation yield depends on the fluence [59], but triggering avalanche ionization also depends on the energy of the photons, which depends on the wavelength following  $E = hc/\lambda$ . The photon energy of a 1030 nm laser pulse is four times lower than that of a 257 nm laser pulse. Multi photon ionization (MPI) [21,22] is then less efficient in NIR than in NUV. In NUV at  $2 \text{ J.cm}^{-2}$ , the photons carried by one pulse have enough energy for triggering ablation following MPI and the possible processes of fragmentation or vaporization [17]. In NIR, the fluence is above the ablation threshold at  $7 \text{ J.cm}^{-2}$  but, due to less energetic photons, a significant fraction of these photons is used within the target lattice to generate local defects, a process named incubation by Seydoux-Guil-laume et al. [60]. Incubation drives to fast ablation when the lattice becomes weak enough against the pulse fluence. This explains the time-resolved signal shapes (Fig. 4) which we explain on Fig. 5. This diagram is the interpretative framework of the crater evolution during ablation based on the time resolved ICP-MS signal, and considering the laser-matter interaction in both NIR and NUV. In the NUV mode, a sharp increase (1) and (2) progressive decrease of the signal intensity are explained by the deterministic (*i.e.* systematic) triggering of ablation and the decrease in fluence inherent to the expansion of the irradiated

surface (Fig. 2). For the first 50 shots, the crater surface develops to  $\approx 6.5 \mu\text{m}$  in depth (Table S2, Appendix) and ablation creates a rough surface (Fig. 2), more favorable to ablation. Meanwhile, the yield increases up to  $> 3000 \text{ c.shot}^{-1}.\text{ppm}^{-1}$ . Beyond 50 shots, the intensity decreases with fluence because the latter, defined as the pulse energy to the irradiated area ratio, decreases quickly. In both NIR modes, the patterns are more complex. The progressive intensity raise (3, 6), and sudden increase (4, 7), before a progressive decrease (5, 8) is explained by the predominance of incubation during the first pulses. The slow intensity increase reflects the low amount of ablated particles. The maximum peak of intensity corresponds to the threshold at which ablation becomes dominant over incubation, and matter removal faster than during the first 30 to 50 shots for IR-S-eq and IR-F-eq, respectively. The following intensity decrease is due to the decrease of fluence with the development of the exposed surface. The difference between intensities in the two NIR modes is explained by the initial fluence which is much lower and close to the ablation threshold in NIR-F-eq than in NIR-S-eq. This interpretation explains the contradictory results which are: (1) similar ablation rates in NUV and NIR over 100 shots (Figs. 3 and 2) different time-resolved signal intensity pattern in NUV and NIR. Indeed, in Fig. 3A, the crater volume from NUV ablation is measurable from 5 to 100 shots, following a linear ablation pattern, whereas the crater volume from NIR ablation is not measurable below 25 shots, which highlights the occurrence of incubation effects.

#### 4.4. Ablation patterns and elemental fractionation

The large amount of rejected U-Pb acquisitions and the higher uncertainties in NIR-F-eq can be linked to elemental fractionation during ablation. Phenomenologically speaking, elemental fractionation can result from incomplete ionization of very large particles in the plasma torch [25] and was invoked in UV fs-LA [8] for fluences close to the ablation threshold. Such near-threshold conditions fit our NIR-F-eq mode, as it shows close to the limit of quantification of  $\text{Pb}^*/\text{U}$  ratios. In addition, Garcia et al. [4] described elemental fractionation as a function of the number of shots, depending on the fluence. Namely, at low fluence, a large amount of shots is needed for stoichiometric sampling to occur. In our study, the low repetition rate that was used (4 Hz) potentially delays the onset of stoichiometric ablation in NIR modes. Fundamentally speaking, the same authors discussed preferential ionization as a source of elemental fractionation. In the NIR modes, photons of lower energy than UV photons are more favorable to the preferential ionization of U against Pb because of the 20% higher first ionization potential of Pb. The subsequent lower amount of measured  $\text{Pb}^*$  would result in younger measured apparent ages and would explain the similar  $\approx 3.5\%$  bias towards younger ages obtained with Plešovice and Mud-tank (Fig. 1 and Table S1, Appendix). Nevertheless, this is not observed with the Fish Canyon Tuff zircon, which is dated accurately against the reference age, or to a lesser extent, *i.e.*  $< 1\%$  of bias towards younger ages (28.31 Ma). The non-linear ablation pattern in NIR and the probabilistic (*i.e.* random) extent of incubation effects may explain why this effect is not as highly reproducible as expected from the theory.

## 5. Conclusion

Near IR and UV wavelengths in fs-LA-ICP-MS were compared in the frame of U-Pb dating of reference zircon materials. The evolution of the crater morphology was studied using high-resolution synchrotron X-ray micro-tomography. Near UV pulse energy realizes ablation of the sample in a deterministic fashion. Near IR laser-matter interactions are more prone to incubation effects due to the lower energy photons as compared to NUV. These effects induced: (1) a nonlinear development of the crater shape because of catastrophic ablation and delayed ablation, (2) a much lower fs-LA-ICP-MS yield than in the NUV mode because only a small fraction of the pulse energy was used to effectively ablate the sample, and (3) a potential role of preferential ionization that

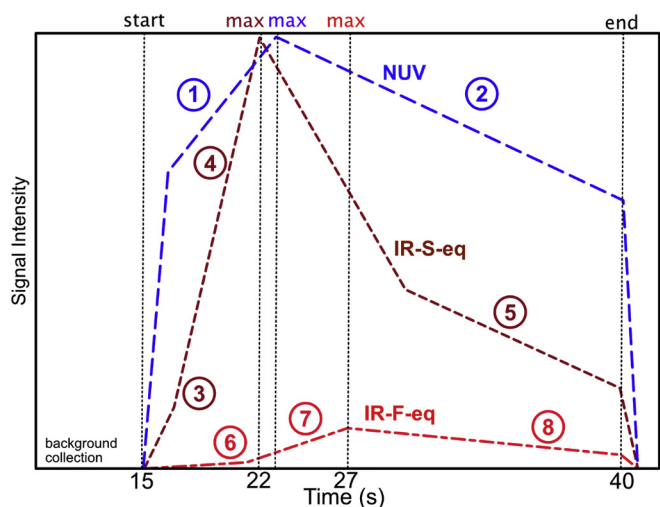


Fig. 5. Interpretative framework of fs-LA in NUV and NIR modes. The intensity scale is adapted to the maximum signal intensity recorded in both the NUV and NIR-S-eq modes. The maximum signal intensity in NIR-F-eq is about ten times as low as that in the NUV mode. The dash lines indicate the start of ablation and the maximum signal peaks. See section 4.3. for description of the stages 1 to 8.

generates elemental fractionation between U and Pb\* at near ablation threshold conditions. In IR-F-eq, several measurements must then be rejected because of a high bias from the Concordia curve (> 15%) or a lack of precision. The remaining dataset is accurate but statistically poor for a robust age estimation. In IR-S-eq mode, *i.e.* at high fluence, the data are statistically robust and accurate, but suffer from high uncertainties relative to the actual expectations from LA-ICP-MS. Finally, NUV is the most powerful mode to obtain statistically robust datasets and its high yield provides room for improvement to increase the actual high spatial resolutions reached for various type of multi-elements analysis, *e.g.* < 10  $\mu\text{m}$  in diameter.

### Declaration of Competing Interest

The authors declare that they have no known competing financial interests or personal relationships that could have appeared to influence the work reported in this paper.

### Acknowledgements

This work was supported by the TelluS program of CNRS/INSU. The Paul Scherrer Institute is acknowledged for provision of synchrotron radiation beamtime at Swiss Light Source, TOMCAT beamline X02DA. Local contact Arttu Miettinen is acknowledged for assistance with image acquisition. The reviewers are thanked for their constructive comments.

### Appendix A. Supplementary data

Supplementary data to this article can be found online at <https://doi.org/10.1016/j.sab.2020.105863>.

### References

- [1] S.P. Chenery, J.M. Cook, Determination of rare earth elements in single mineral grains by laser ablation microprobe – inductively coupled plasma mass spectrometry: preliminary study, *J. Anal. At. Spectrom.* 8 (1993) 299–303, <https://doi.org/10.1039/JA9308000299>.
- [2] S.E. Jackson, H.P. Longrich, G.R. Dunning, B.J. Fryer, The application of laser-ablation microprobe - inductively coupled plasma - mass-spectrometry (LAM-ICP-MS) to *in situ* trace-element determinations in minerals, *Can. Mineral.* 30 (1992) 1049–1064.
- [3] M. Motelica-Heino, S. Rauch, G. Morrison, O.F. Donard, Determination of palladium, platinum and rhodium concentrations in urban road sediments by laser ablation-ICP-MS, *Anal. Chim. Acta* 436 (2001) 233–244, [https://doi.org/10.1016/S0003-2670\(01\)00967-9](https://doi.org/10.1016/S0003-2670(01)00967-9).
- [4] C.C. Garcia, H. Lindner, A. von Bohlen, C. Vadla, K. Niemax, Elemental fractionation and stoichiometric sampling in femtosecond laser ablation, *J. Anal. At. Spectrom.* 23 (2008) 470–478 <https://doi.org/10.1039/b718845e>.
- [5] J. Bonse, J.M. Wrobel, J. Krüger, W. Kautek, Ultrashort-pulse laser ablation of indium phosphide in air, *Appl. Phys. A Mater. Sci. Process.* 72 (2001) 89–94 <https://doi.org/10.1007/s003390000596>.
- [6] B. Fernandez, F. Claverie, C. Pecheyran, O.F.X. Donard, Direct analysis of solid samples by fs-LA-ICP-MS, *Trends Anal. Chem.* 26 (2007) 951–965, <https://doi.org/10.1016/j.trac.2007.08.008>.
- [7] F. Claverie, B. Fernández, C. Pecheyran, J. Alexis, O.F.X. Donard, Elemental fractionation effects in high repetition rate IR femtosecond laser ablation ICP-MS analysis of glasses, *J. Anal. At. Spectrom.* 24 (2009) 891, <https://doi.org/10.1039/b904134f>.
- [8] J. Koch, M. Wälle, J. Pisonero, Performance characteristics of ultra-violet femtosecond laser ablation inductively coupled plasma mass spectrometry at ~265 and ~200 nm, *J. Anal. At. Spectrom.* 21 (2006) 932–940 <http://www.rsc.org/Publishing/Journals/JA/article.asp?doi=b603929d>.
- [9] K. Niemax, Laser ablation - reflections on a very complex technique for solid sampling, *Fresenius J. Anal. Chem.* 370 (2001) 332–340 <https://doi.org/10.1007/s002160100796>.
- [10] R. Hergenröder, O. Samek, V. Hommes, Femtosecond laser ablation elemental mass spectrometry, *Mass Spectrom. Rev.* 25 (2006) 551–572 <https://doi.org/10.1002/mas.20077>.
- [11] T.E. Jeffries, S.E. Jackson, H.P. Longrich, Application of a frequency quintupled Nd:YAG source ( $\lambda = 213\text{ nm}$ ) for laser ablation inductively coupled plasma mass spectrometric analysis of minerals, *J. Anal. At. Spectrom.* 13 (1998) 935–940, <https://doi.org/10.1039/A801328D>.
- [12] R.E. Russo, X.L. Mao, O.V. Borisov, H. Liu, Influence of wavelength on fractionation in laser ablation ICP-MS, *J. Anal. At. Spectrom.* 15 (2000) 1115–1120, <https://doi.org/10.1039/b004243i>.
- [13] R.E. Russo, X. Mao, H. Liu, J. Gonzalez, S.S. Mao, Laser ablation in analytical chemistry—a review, *Talanta* 57 (2002) 425–451, [https://doi.org/10.1016/S0039-9140\(02\)00053-X](https://doi.org/10.1016/S0039-9140(02)00053-X).
- [14] J. Gonzalez, X.L. Mao, J. Roy, S.S. Mao, R.E. Russo, Comparison of 193, 213 and 266 nm laser ablation ICP-MS, *J. Anal. At. Spectrom.* 17 (2002) 1108–1113 <https://doi.org/10.1039/b202122f>.
- [15] M. Guillon, I. Horn, D. Günther, A comparison of 266 nm, 213 nm and 193 nm produced from a single solid state Nd : YAG laser for laser ablation ICP-MS, *J. Anal. At. Spectrom.* 18 (2003) 1224–1230, <https://doi.org/10.1039/b305434a>.
- [16] I. Horn, M. Guillon, D. Günther, Wavelength dependant ablation rates for metals and silicate glasses using homogenized laser beam profiles — implications for LA-ICP-MS, *Appl. Surf. Sci.* 182 (2001) 91–102, [https://doi.org/10.1016/S0169-4332\(01\)00465-2](https://doi.org/10.1016/S0169-4332(01)00465-2).
- [17] D. Perez, L.J. Lewis, Molecular-dynamics study of ablation of solids under femtosecond laser pulses, *Phys. Rev. B* 67 (2003) 184102, <https://doi.org/10.1103/PhysRevB.67.184102>.
- [18] F. Poitrasson, X. Mao, S.S. Mao, R. Freyrier, R.E. Russo, Comparison of ultraviolet femtosecond and nanosecond laser ablation inductively coupled plasma mass spectrometry analysis in glass, monazite, and zircon, *Anal. Chem.* 75 (2003) 6184–6190, <https://doi.org/10.1021/ac034680a>.
- [19] V. Mozna, J. Pisonero, M. Hola, V. Kanicky, D. Günther, Quantitative analysis of Fe-based samples using ultraviolet nanosecond and femtosecond laser ablation-ICP-MS, *J. Anal. At. Spectrom.* 21 (2006) 1194–1201, <https://doi.org/10.1039/B606988F>.
- [20] D. Du, X. Liu, G. Korn, J. Squier, G. Mourou, Laser-induced breakdown by impact ionization in SiO<sub>2</sub> with pulse widths from 7ns to 150fs, *Appl. Phys. Lett.* 64 (1994) 3071–3073, <https://doi.org/10.1063/1.111350>.
- [21] M. Lenzner, J. Krüger, S. Sartania, Z. Cheng, C. Spielmann, G. Mourou, W. Kautek, F. Krausz, Femtosecond optical breakdown in dielectrics, *Phys. Rev. Lett.* 80 (1998) 4076, <https://doi.org/10.1103/PhysRevLett.80.4076>.
- [22] B.C. Stuart, M.D. Feit, S. Herman, A.M. Rubenchik, B.W. Shore, M.D. Perry, Nanosecond-to-femtosecond laser-induced breakdown in dielectrics, *Phys. Rev. B* 53 (1996) 1749–1761, <https://doi.org/10.1016/j.sab.2007.03.034>.
- [23] P. Lorazo, L.J. Lewis, M. Meunier, Short-pulse laser ablation of solids: from phase explosion to fragmentation, *Phys. Rev. Lett.* 91 (2003) 225502 <http://link.aps.org/abstract/PRL/v91/e225502>.
- [24] K. Yamada, W. Watanabe, T. Toma, K. Itoh, J. Nishii, In situ observation of photoinduced refractive-index changes in filaments formed in glasses by femtosecond laser pulses, *Opt. Lett.* 26 (2001) 19–21 <http://ol.osa.org/abstract.cfm?URI=ol-26-1-19>.
- [25] I. Horn, F. von Blanckenburg, Investigation on elemental and isotopic fractionation during 196 nm femtosecond laser ablation multiple collector inductively coupled plasma mass spectrometry, *Spectrochim. Acta Part B At. Spectrosc.* 62 (2007) 410–422, <https://doi.org/10.1016/j.sab.2007.03.034>.
- [26] J. Chmeleff, I. Horn, G. Steinhofel, F. von Blanckenburg, In situ determination of precise stable Si isotope ratios by UV-femtosecond laser ablation high-resolution multi-collector ICP-MS, *Chem. Geol.* 249 (2008) 155–166, <https://doi.org/10.1016/j.chemgeo.2007.12.003>.
- [27] F.-X. D'Abzac, F. Poitrasson, R. Freyrier, A.-M. Seydoux-Guillaume, Near infra red femtosecond laser ablation: the influence of energy and pulse width on the LA-ICP-MS analysis of monazite, *J. Anal. At. Spectrom.* 25 (2010) 681–689, <https://doi.org/10.1039/b913584g>.
- [28] T. Hirata, T. Ohno, In-situ isotopic ratio analysis of iron using laser ablation-multiple collector-inductively coupled plasma mass spectrometry (LA-MC-ICP-MS), *J. Anal. At. Spectrom.* 16 (2001) 487–491, <https://doi.org/10.1039/b100946j>.
- [29] F.-X. d'Abzac, B.L. Beard, A.D. Czaja, H. Konishi, J.J. Schauer, C.M. Johnson, Iron isotope composition of particles produced by UV-femtosecond laser ablation of natural oxides, sulfides, and carbonates, *Anal. Chem.* 85 (2013) 11885–11892, <https://doi.org/10.1021/ac402722t>.
- [30] F.-X. d'Abzac, A.D. Czaja, B.L. Beard, J.J. Schauer, C.M. Johnson, Iron distribution in size-resolved aerosols generated by UV-femtosecond laser ablation: influence of cell geometry and implications for in situ isotopic determination by LA-MC-ICP-MS, *Geostand. Geoanal. Res.* 38 (2014) 293–309, <https://doi.org/10.1111/j.1751-908X.2014.00281.x>.
- [31] F.-X. D'Abzac, A.-M. Seydoux-Guillaume, J. Chmeleff, L. Datas, F. Poitrasson, In situ characterization of infra red femtosecond laser ablation in geological samples. Part B: the laser induced particles, *J. Anal. At. Spectrom.* 27 (2012) 108, <https://doi.org/10.1039/c1ja10154d>.
- [32] S.E. Jackson, N.J. Pearson, W.L. Griffin, E.A. Belousova, The application of laser ablation-inductively coupled plasma-mass spectrometry to *in situ* U-Pb zircon geochronology, *Chem. Geol.* 211 (2004) 47–69.
- [33] M.S.A. Horstwood, J. Košler, G. Gehrels, S.E. Jackson, N.M. McLean, C. Paton, N.J. Pearson, K. Sircombe, P. Sylvester, V. Vermeesch, J.F. Bowring, D.J. Condon, B. Schoene, Community-derived standards for LA-ICP-MS U-(Th)-Pb geochronology - uncertainty propagation, age interpretation and data reporting, *Geostand. Geoanal. Res.* 40 (2016) 311–332, <https://doi.org/10.1111/j.1751-908X.2016.00379.x>.
- [34] J.L. Paquette, M. Tiepolo, High resolution (5  $\mu\text{m}$ ) U-Th-Pb isotope dating of monazite with excimer laser ablation (ELA)-ICPMS, *Chem. Geol.* 240 (2007) 222–237, <https://doi.org/10.1016/j.chemgeo.2007.02.014>.
- [35] D.M. Chew, P.J. Sylvester, M.N. Tubrett, U-Pb and Th-Pb dating of apatite by LA-ICPMS, *Chem. Geol.* 280 (2011) 200–216, <https://doi.org/10.1016/J.CHEMGEO.2010.11.010>.
- [36] J. Kosler, Laser ablation ICP-MS – a new dating tool in earth science, *Proc. Geol. Assoc.* 118 (2007) 19–24, [https://doi.org/10.1016/S0016-7878\(07\)80043-5](https://doi.org/10.1016/S0016-7878(07)80043-5).



- [37] G. Martínez-Criado, R. Tucoulou, P. Cloetens, P. Bleuet, S. Bohic, J. Cauzid, I. Kieffer, E. Kosior, S. Labouré, S. Petitgirard, A. Rack, J.A. Sans, J. Segura-Ruiz, H. Suhonen, J. Susini, J. Villanova, IUCr, status of the hard X-ray microprobe beamline ID22 of the European Synchrotron Radiation Facility, *J. Synchrotron Radiat.* 19 (2012) 10–18, <https://doi.org/10.1107/S090904951104249X>.
- [38] M. Wiedenbeck, P. Allé, F. Corfu, W.L. Griffin, M. Meier, F. Oberli, A. Von Quadt, J.C. Roddick, W. Spiegel, Three natural zircon standards for U-Th-Pb, Lu-Hf, trace element and REE analyses, *Geostand. Geoanal. Res.* 19 (1995) 1–23 <https://doi.org/10.1111/j.1751-908X.1995.tb00147.x>.
- [39] J. Sláma, J. Košler, D.J. Condon, J.L. Crowley, A. Gerdes, J.M. Hanchar, M.S.A. Horstwood, G.A. Morris, L. Nasdala, N. Norberg, U. Schaltegger, B. Schoene, M.N. Tubrett, M.J. Whitehouse, Plešovice zircon — a new natural reference material for U-Pb and Hf isotopic microanalysis, *Chem. Geol.* 249 (2008) 1–35 <https://doi.org/10.1016/j.chemgeo.2007.11.005>.
- [40] M.D. Schmitz, S.A. Bowring, U-Pb zircon and titanite systematics of the fish canyon tuff: an assessment of high-precision U-Pb geochronology and its application to young volcanic rocks, *Geochim. Cosmochim. Acta* 65 (2001) 2571–2587, [https://doi.org/10.1016/S0016-7037\(01\)00616-0](https://doi.org/10.1016/S0016-7037(01)00616-0).
- [41] L.P. Black, B.L. Gulson, The age of the mud tank carbonatite, Strangways range, Northern Territory, *J. Aust. Geol. Geophys.* 3 (1978) 227–232.
- [42] J.-P. Suuronen, M. Sayab, 3D nanopetrography and chemical imaging of datable zircons by synchrotron multimodal X-ray tomography, *Sci. Rep.* 8 (2018) 4747, <https://doi.org/10.1038/s41598-018-22891-9>.
- [43] J. Michel, L. Baumgartner, B. Putlitz, U. Schaltegger, M. Ovtcharova, Incremental growth of the Patagonian Torres del Paine laccolith over 90 k.y., *Geology*. 36 (2008) 459, <https://doi.org/10.1130/G24546A.1>.
- [44] F. Poitrasson, F.-X. D'Abzac, Femtosecond laser ablation inductively coupled plasma source mass spectrometry for elemental and isotopic analysis: Are ultrafast lasers worthwhile? *J. Anal. At. Spectrom.* 32 (2017), <https://doi.org/10.1039/c7ja00084g>.
- [45] C. Paton, J.D. Woodhead, J.C. Hellstrom, J.M. Hergt, A. Greig, R. Maas, Improved laser ablation U-Pb zircon geochronology through robust downhole fractionation correction, *Geochem. Geophys. Geosyst.* 11 (2010), <https://doi.org/10.1029/2009GC002618> n/a-n/a.
- [46] M. Stambanoni, A. Groso, A. Isenegger, G. Mikuljan, Q. Chen, A. Bertrand, S. Henein, R. Betemps, U. Frommherz, P. Böhrer, D. Meister, M. Lange, R. Abela, Trends in synchrotron-based tomographic imaging: the SLS experience, in: U. Bonse (Ed.), *International Society for Optics and Photonics*, 2006, <https://doi.org/10.1117/12.679497> (p. 63180M).
- [47] F. Marone, M. Stambanoni, IUCr, Regridding reconstruction algorithm for real-time tomographic imaging, *J. Synchrotron Radiat.* 19 (2012) 1029–1037, <https://doi.org/10.1107/S0909049512032864>.
- [48] I. Pitas, *Digital Image Processing Algorithms and Applications*, Wiley, 2000.
- [49] G.A. Cowan, H.H. Adler, The variability of the natural abundance of <sup>235</sup>U, *Geochim. Cosmochim. Acta* 40 (1976) 1487–1490, [https://doi.org/10.1016/0016-7037\(76\)90087-9](https://doi.org/10.1016/0016-7037(76)90087-9).
- [50] O.V. Borisov, X. Mao, R.E. Russo, Effects of crater development on fractionation and signal intensity during laser ablation inductively coupled plasma mass spectrometry, *Spectrochim. Acta Part B At. Spectrosc.* 55 (2000) 1693–1704, [https://doi.org/10.1016/S0584-8547\(00\)00272-X](https://doi.org/10.1016/S0584-8547(00)00272-X).
- [51] A. Ben-Yakar, A. Harkin, J. Ashmore, R.L. Byer, H.A. Stone, Thermal and fluid processes of a thin melt zone during femtosecond laser ablation of glass: the formation of rims by single laser pulses, *J. Phys. D-Appl. Phys.* 40 (2007) 1447–1459, <https://doi.org/10.1088/0022-3727/40/5/021>.
- [52] R. Le Harzic, N. Huot, E. Audouard, C. Jonin, P. Laporte, S. Valette, A. Frackiewicz, R. Fortunier, Comparison of heat-affected zones due to nanosecond and femtosecond laser pulses using transmission electronic microscopy, *Appl. Phys. Lett.* 80 (2002) 3886–3888, <https://doi.org/10.1063/1.1481195>.
- [53] D. von der Linde, H. Schüler, Breakdown threshold and plasma formation in femtosecond laser–solid interaction, *J. Opt. Soc. Am. Part B.* 13 (1996) 216–222, <https://doi.org/10.1364/JOSAB.13.000216>.
- [54] S. Butkus, E. Gaižauskas, D. Paipulas, Ž. Vibury, D. Kaškelyė, M. Barkauskas, A. Alesnikov, V. Sirutkaitis, Rapid microfabrication of transparent materials using filamented femtosecond laser pulses, *Appl. Phys. A Mater. Sci. Process.* 114 (2014) 81–90, <https://doi.org/10.1007/s00339-013-8108-2>.
- [55] T.E. Jeffries, W.T. Perkins, N.J.G. Pearce, Comparisons of infrared and ultraviolet laser probe microanalysis inductively coupled plasma mass spectrometry in mineral analysis, *Analyst.* 120 (1995) 1365, <https://doi.org/10.1039/an9952001365>.
- [56] C.C. Garcia, H. Lindner, K. Niemax, Transport efficiency in femtosecond laser ablation inductively coupled plasma mass spectrometry applying ablation cells with short and long washout times, *Spectrochim. Acta Part B-Atomic Spectrosc.* 62 (2007) 13–19, <https://doi.org/10.1016/j.sab.2006.11.005>.
- [57] J. Koch, S. Schlamp, T. Rösger, D. Fliegel, D. Günther, Visualization of aerosol particles generated by near infrared nano- and femtosecond laser ablation, *Spectrochim. Acta Part B At. Spectrosc.* 62 (2007) 20–29, <https://doi.org/10.1016/j.sab.2006.11.006>.
- [58] X.-Y. Zheng, B.L. Beard, S. Lee, T.R. Reddy, H. Xu, C.M. Johnson, Contrasting particle size distributions and Fe isotope fractionations during nanosecond and femtosecond laser ablation of Fe minerals: implications for LA-MC-ICP-MS analysis of stable isotopes, *Chem. Geol.* 450 (2017) 235–247, <https://doi.org/10.1016/J.CHEMGEO.2016.12.038>.
- [59] S. Nolte, C. Momma, H. Jacobs, A. Tünnermann, B.N. Chichkov, B. Wellegehausen, H. Welling, Ablation of metals by ultrashort laser pulses, *J. Opt. Soc. Am. B.* 14 (1997) 2716–2722, <https://doi.org/10.1364/JOSAB.14.002716>.
- [60] A.M. Seydoux-Guillaume, R. Freydisier, F. Poitrasson, F.X. D'Abzac, R. Wirth, L. Datas, Dominance of mechanical over thermally induced damage during femtosecond laser ablation of monazite, *Eur. J. Mineral.* (2010), <https://doi.org/10.1127/0935-1221/2010/0022-2001%0A>.